Editors' Suggestion

Emergence of a Symmetry-Broken Chern Insulator near a Moiré Kondo Breakdown

Wanghao Tian,[1,*] Bowen Shen,[2,3,*] Lizhong Li,[2,3] Mingjie Zhang,[4] Feng Liu,[1] Chushan Li,[1,5] Yaotian Liu,[4] Fan Xu,[1,5] Kenji Watanabe,[6] Takashi Taniguchi,[7] Peiling Li,[4] Li Lu,[4,8] Yang Xu,[4] Shengwei Jiang,[1,5,†] Tingxin Li,[1,5,8,‡] Jie Shan,[2,3,9,§] and Kin Fai Mak[2,3,9,‖]

[1]*State Key Laboratory of Micro-nano Engineering Science, Key Laboratory of Artificial Structures and Quantum Control (Ministry of Education), School of Physics and Astronomy, Shanghai Jiao Tong University, Shanghai, China*
[2]*School of Applied and Engineering Physics and Laboratory of Atomic and Solid State Physics, Cornell University, Ithaca, New York, USA*
[3]*Kavli Institute at Cornell for Nanoscale Science, Ithaca, New York, USA*
[4]*Beijing National Laboratory for Condensed Matter Physics and Institute of Physics, Chinese Academy of Sciences, Beijing, China*
[5]*Tsung-Dao Lee Institute, Shanghai Jiao Tong University, Shanghai, China*
[6]*Research Center for Electronic and Optical Materials, National Institute for Materials Science, 1-1 Namiki, Tsukuba, Japan*
[7]*Research Center for Materials Nanoarchitectonics, National Institute for Materials Science, 1-1 Namiki, Tsukuba, Japan*
[8]*Hefei National Laboratory, Hefei, China*
[9]*Max Planck Institute for the Structure and Dynamics of Matter, Hamburg, Germany*

(Received 18 February 2026; revised 7 August 2026; accepted 13 October 2026; published 13 November 2026)

Moiré semiconductors built on angle-aligned transition metal dichalcogenide (TMD) heterobilayers provide a physical realization of the Kondo lattice model, in which one TMD layer is prepared in a Mott insulating state supporting a lattice of local magnetic moments and the other layer in a metallic state supporting itinerant carriers. The artificial Kondo lattice enables the exploration of exotic states of matter near a continuously tunable Kondo breakdown. Here we report the emergence of a symmetry-broken Chern insulator at a moiré hole filling factor $4/3$ in angle-aligned $MoTe_2/WSe_2$ moiré bilayers, which realize a chiral Kondo lattice. The symmetry-broken Chern insulator, which exhibits integer quantized Hall conductance at a fractional moiré filling, breaks the translational symmetry of the lattice spontaneously; it also appears only near a magnetic-field-induced Kondo breakdown in the mixed-valence regime of the material. We further demonstrate that the magnetic field required to induce the Kondo breakdown and to stabilize the symmetry-broken Chern insulator is twist angle dependent. The results present new opportunities for exploring the subtle interplay between topology and Kondo interactions in moiré semiconductors.

DOI: 10.1103/szcj-44xj

Introduction—The Kondo lattice, a lattice of localized magnetic moments coupled via exchange interactions to a sea of itinerant electrons, is a prototypical strongly correlated system [1,2]. Driven by the strong Coulomb repulsion and the Kondo interaction, the system can host a suite of quantum phases of matter, such as heavy Fermi liquids [3,4], Kondo insulators [5,6], quantum critical non-Fermi liquids [7–9], and unconventional superconductivity [10–12]. Whereas Kondo lattice physics has been extensively studied in lanthanide and actinide intermetallic compounds [13–16], the emergence of two-dimensional semiconducting moiré materials has presented a new platform to study the Kondo lattice problem in a continuously tunable manner [17–26]. In particular, varying the moiré lattice filling factor and/or an electric field perpendicular to the sample plane in these materials can tune the effective Kondo interaction and induce a breakdown of the Kondo singlets, near where exotic states of matter could emerge.

In this Letter, we report the experimental observation of a symmetry-broken Chern insulator at a moiré hole filling factor $\nu = 4/3$ and near a magnetic-field-induced Kondo breakdown in dual-gated devices of angle-aligned $MoTe_2/WSe_2$ moiré bilayers [Fig. 1(a)]. The top and bottom gates in these devices allow independent tuning of ν and the vertical electric field E. (See Supplemental Material [27] for details on device fabrication and electrical transport measurements.) Recent scanning transmission electron microscopy experiments [28] have clarified that the angle-aligned $MoTe_2/WSe_2$ bilayers previously

*These authors contributed equally to this work.
†Contact author: swjiang@sjtu.edu.cn
‡Contact author: txli89@sjtu.edu.cn
§Contact author: jie.shan@mpsd.mpg.de
‖Contact author: kin-fai.mak@mpsd.mpg.de

Published by the American Physical Society under the terms of the Creative Commons Attribution 4.0 International license. Further distribution of this work must maintain attribution to the author(s) and the published article's title, journal citation, and DOI. Open access publication funded by the Max Planck Society.

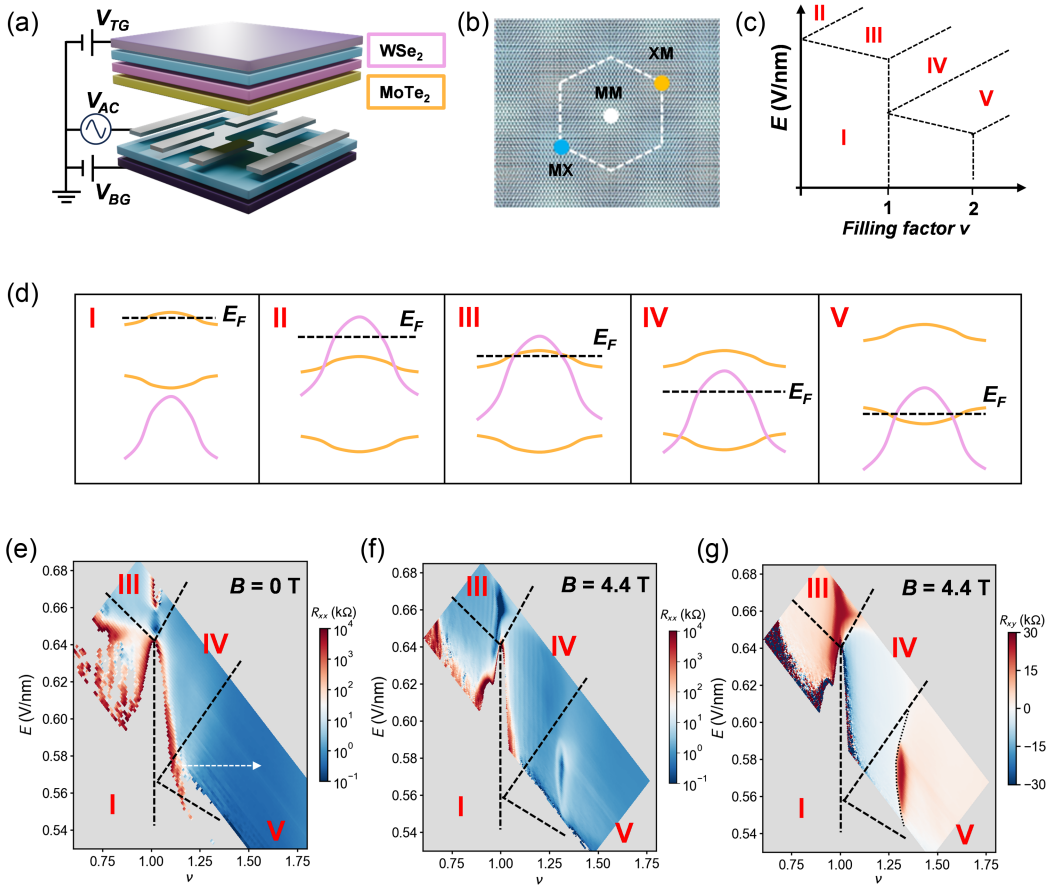


FIG. 1. Electrostatics phase diagram of angle-aligned $MoTe_2/WSe_2$ bilayers. (a) Schematic dual-gated Hall bar device of an angle-aligned $MoTe_2/WSe_2$ moiré bilayer. (b) Schematic moiré lattice formed by the lattice-mismatched TMD layers, showing the three high-symmetry stacking sites (MM, MX, XM). (c) Schematic electrostatics phase diagram as a function of the hole filling factor ν and the perpendicular electric field E. Five distinct regions (I–V) are separated by dashed lines. (d) Schematic band alignment in regions I–V, where the pink and yellow colors correspond to the WSe_2 moiré band and the $MoTe_2$ Hubbard bands, respectively. The Fermi level is denoted by a dashed line. (e),(f) Longitudinal resistance R_{xx} as a function of ν and E at perpendicular magnetic fields $B = 0$ T (e) and 4.4 T (f). (g) The corresponding antisymmetrized Hall resistance R_{xy} at $B = 4.4$ T. The dashed lines mark the boundaries separating the different regions, and the dotted line marks the Kondo breakdown boundary, where R_{xy} changes sign. A pronounced R_{xy} hot spot together with an R_{xx} dip emerges at $\nu = 4/3$ in the mixed-valence region (region V). All data were taken at a lattice temperature $T = 20$ mK.

shown to host a topologically nontrivial Chern band [18–22,29–31] are AA-stacked rather than AB-stacked. Consequently, the hexagonal moiré lattice features three high-symmetry stacking sites: MM, MX, and XX, where M represents Mo or W and X denotes Te or Se [Fig. 1(b)]. The 7% lattice mismatch between the Mo and W layer gives a moiré period $a_M \approx 4.8$ nm and a moiré density $n_M \approx 4.5 \times 10^{12}$ cm^{-2}. The Wannier orbitals of the Mo and W layer are centered at the two sublattice sites of the lattice; the sublattice potential and thus the energy separation between the Mo- and W-moiré bands are continuously tunable by the electric field E.

Electrostatics phase diagram—Figure 1(c) shows a schematic phase diagram of the material, which can be separated into five different regions (I–V) with boundaries marked by dashed lines, as reported in previous studies [18–22]. The corresponding band alignment between the two layers is shown in Fig. 1(d). In region I, only the Mo layer is hole doped with a moiré hole filling factor $\nu = \nu_{\mathrm{Mo}} + \nu_{\mathrm{W}} = \nu_{\mathrm{Mo}} + 0$ (here ν_{Mo} and ν_{W} denote the hole filling factor in the Mo and W layer, respectively). Insulating states were reported at $\nu_{\mathrm{Mo}} = 1$ and 2 corresponding to a Mott and a band insulator, respectively [18,22,29]. As a result of the strong on-site Coulomb repulsion (U) compared to the bandwidth in the Mo layer, the topmost Mo-moiré band is split into the lower and upper Hubbard bands. Similarly, only the topmost W-moiré band is hole doped in region II, i.e., $\nu = 0 + \nu_{\mathrm{W}}$. Because of the substantially larger bandwidth in the W layer, no insulating state can be identified at $\nu_{\mathrm{W}} = 1$, demonstrating that holes in the W layer are much less correlated than those in the Mo layer [22].

Region IV corresponds to the Kondo lattice region. Here the Mo layer is kept at the Mott insulating state (i.e.,

$\nu_{\mathrm{Mo}} = 1$) supporting a triangular lattice of local magnetic moments; the Mott gap size is proportional to the electric field span in this region [18]. The W layer hosts a sea of itinerant holes with tunable density ν_{W}; the total hole filling is $\nu = 1 + \nu_{\mathrm{W}}$. The low-energy physics in this region can be mapped to a chiral Kondo lattice model carrying an exchange interaction (J) between the local moments in the Mo layer, an intralayer hopping term (t) for the itinerant holes in the W layer, and a Kondo exchange interaction (J_K) between the spins in the Mo and W layer; J_K further carries a p-wave chiral form factor that gives rise to a topologically nontrivial Kondo hybridization gap [23]. The emergence of chiral Kondo lattice physics in this region is supported by the observation [18,21,22] of (1) a tunable heavy Fermi liquid, (2) a Kondo breakdown (induced by magnetic field or by variation in ν_{W}) from a heavy Fermi liquid with density $1 + \nu_{\mathrm{W}}$ to an itinerant Fermi liquid with density ν_{W} decoupled from the local moments, (3) a Chern metal near the Kondo breakdown, and (4) a topological Kondo insulator at $\nu = 1 + 1$.

Outside the Kondo lattice region, the material enters the mixed-valence regions (III and V). The upper (lower) part corresponds to $\nu = \nu_{\mathrm{Mo}} + \nu_{\mathrm{W}}$ with $\nu_{\mathrm{Mo}} < 1$ in region III ($\nu_{\mathrm{Mo}} > 1$ in region V). The hole Fermi level cuts through both the W-moiré band and the Mo-Hubbard band here; only the singly occupied sites in the Mo layer carry local magnetic moments; the local-moment density is strongly fluctuating. We will focus on region V in this study, where the Fermi level cuts through the W-moiré band and the Mo upper Hubbard band.

Emergence of a symmetry-broken Chern insulator at $v = 4/3$—Figures 1(e) and 1(f) show the longitudinal resistance (R_{xx}) of device I (with nearly perfect angle alignment, i.e., $a_M \approx 4.8$ nm and $n_M \approx 4.6 \times 10^{12}$ cm^{-2}) as a function of ν and E at a perpendicular magnetic field $B = 0$ and 4.4 T, respectively. The corresponding Hall resistance (R_{xy}) map at $B = 4.4$ T is shown in Fig. 1(g). Unless otherwise specified, the measurement temperature for device I is at a lattice temperature $T = 20$ mK. The gray-shaded areas are the inaccessible regions in the phase diagram due to limited gate voltage range and/or large contact or sample resistance. The dashed lines mark the phase boundaries for regions I, III, and IV as discussed above.

As shown in Fig. 1(e), an electric-field-induced phase transition from a Mott insulator to a quantum anomalous Hall (QAH) insulator and then to an antiferromagnetic insulator was observed at $\nu = 1$ and $B = 0$ T, in agreement with previous studies [22,29,31]. At $B = 4.4$ T [Fig. 1(f)], vertical stripes of Shubnikov–de Haas (SdH) oscillations are observed in region IV; they help to identify the phase boundaries marked by black dashed lines. The oscillations originate from the Landau levels in the W layer after a magnetic-field-induced Kondo breakdown. Moreover, $R_{xy}(< 0)$ corresponds to a hole Fermi surface with density ν_{W} in most of the accessible area within region IV. These results demonstrate the emergence of an itinerant hole gas in the W layer after the Kondo breakdown; the hole gas is decoupled from the Mott insulator in the Mo layer. These observations are fully consistent with earlier reports on the same material [18–22].

The most striking observation is the emergence of an R_{xx} dip (surrounded by an enhanced R_{xx}) and an R_{xy} hot spot at $\nu \approx 4/3$ under $B = 4.4$ T in region V (the lower part of the mixed-valence region). The state spans a finite electric field range in the region. The R_{xy} hot spot is also located near a boundary, where R_{xy} changes sign [dotted line in Fig. 1(g)]. Note that the R_{xx} dip and R_{xy} hot spot in region III correspond to the QAH state at $\nu = 1$.

We further investigate the nature of the $\nu = 4/3$ state. Figures 2(a) and 2(b) show R_{xx} and R_{xy}, respectively, as a function of ν and B at $E = 0.575$ V/nm. The electric field is chosen near the center of the $\nu = 4/3$ state as shown in Fig. 1(g). The R_{xx} dip and R_{xy} hot spot near $\nu = 4/3$ start to appear at $B \approx 2$ T. A sign change in R_{xy} is also observed at a critical magnetic field (B_C); B_C increases monotonically with ν, and the $\nu = 4/3$ state disappears abruptly at $B_C \approx 4.7$ T for device I. A set of Landau fans originating from $\nu = 1$ also appears for $B > B_C$.

Figure 2(c) shows a representative line cut at $B = 4.4$ T. A quantized R_{xy} at (h/e^2) accompanied by an R_{xx} dip (down to about 200 Ω) is observed at $\nu = 4/3$. We also show in Fig. 2(d) the magnetic field dependence of R_{xx} and R_{xy} along the dashed line in Figs. 2(a) and 2(b). R_{xy} increases quickly above $B \approx 2$ T, becomes nearly quantized at (h/e^2) for $3 \lesssim B \lesssim 5$ T, and abruptly decreases in magnitude and changes sign at B_C. Accompanied by this is the appearance of R_{xx} peaks at $B \approx 2$ and 5 T and a vanishing R_{xx} in between.

The integer quantized $R_{xy} = (h/e^2)$ and the vanishing R_{xx} at a fractional filling $\nu = 4/3$ demonstrate the emergence of a symmetry-broken Chern insulating state, or equivalently, a topological charge density wave state [31–40]. The conclusion is further supported by the dispersion of the $\nu = 4/3$ state with magnetic field. The slope of the dispersion follows the Streda formula $n_M(d\nu/dB) = C(e/h)$ with a Chern number close to $C = -1$ (dashed lines). The symmetry-broken Chern insulator appears only in a narrow field window of $2 \lesssim B \lesssim 5$ T. It is not an integer quantum Hall state as it is not part of the Landau fan that appears at $B \gtrsim B_C$; the abrupt disappearance of the state at B_C is also inconsistent with a quantum Hall state. The energy gap of the symmetry-broken Chern insulator can be estimated by the temperature dependence of R_{xx} and R_{xy} (at $B = 4.4$ T) shown in Fig. 2(e). The quantized Hall transport disappears at a temperature around 1 K [Fig. 2(e) and Supplemental Material Fig. 1 [27]]. A thermal activation fit [Fig. 2(f)] to the R_{xx} temperature dependence gives an energy gap of about 0.25 meV (or 3 K).

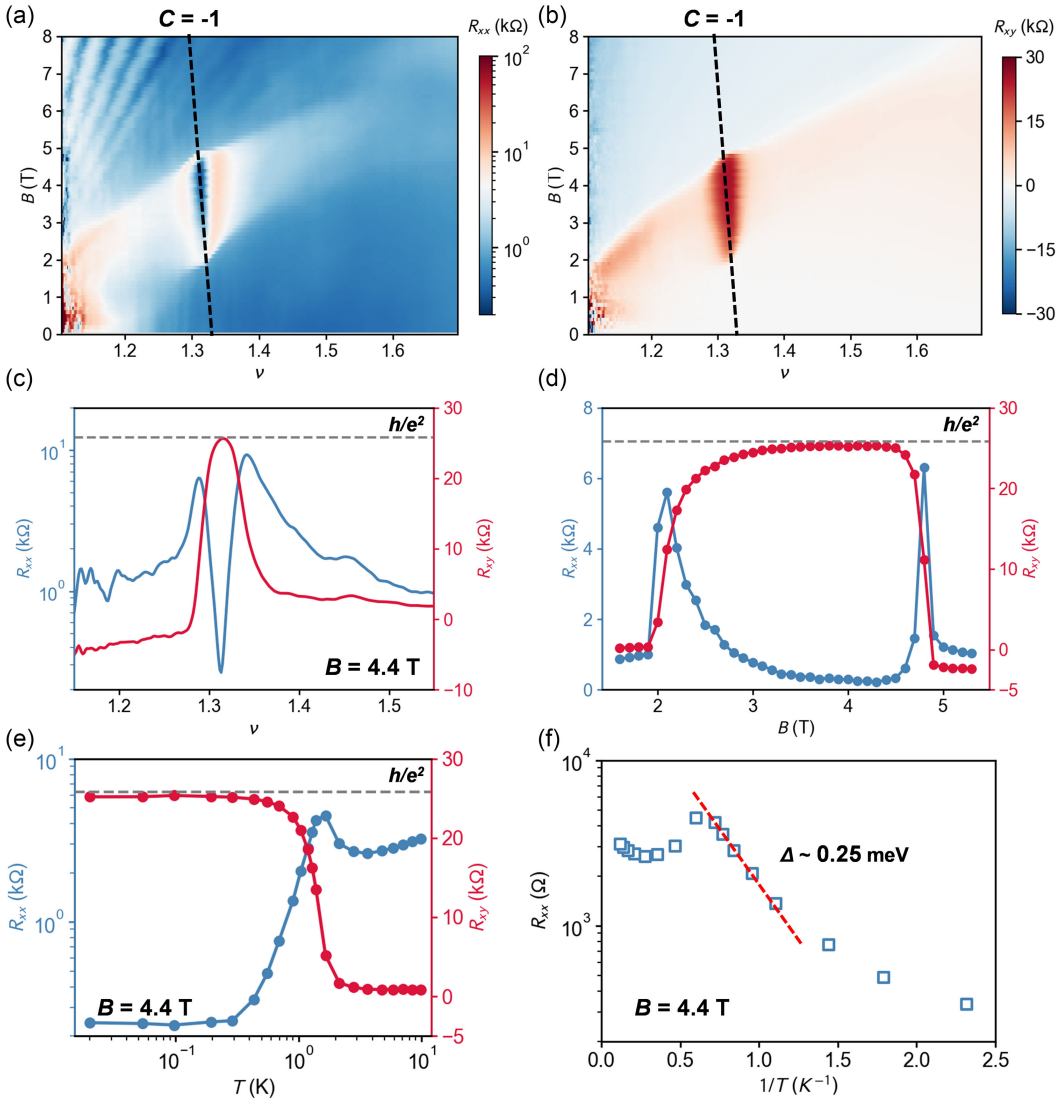


FIG. 2. Symmetry-broken Chern insulator at $\nu = 4/3$. (a) R_{xx} and (b) R_{xy} as a function of ν and B at a fixed electric field $E = 0.575$ V/nm [along the dashed arrow in Fig. 1(e)]. The dashed line marks the dispersion of a $C = -1$ Chern insulator based on the Streda formula. (c) Line cut of R_{xx} (blue) and R_{xy} (red) at $B = 4.4$ T, showing a quantized Hall resistance (h/e^2) and a concomitant R_{xx} dip at $\nu = 4/3$. (d) R_{xx} and R_{xy} as functions of B along the dashed line in (a) and (b). The Hall resistance is nearly quantized for $3 \lesssim B \lesssim 5$ T and changes sign abruptly at the critical field $B_C \approx 4.7$ T. (e) Temperature dependence of R_{xx} and R_{xy} at $\nu = 4/3$ and $B = 4.4$ T. (f) Arrhenius plot of R_{xx} yielding an energy gap about 0.25 meV (3 K). The dashed line is a thermal-activation fit.

Relationship between the $\nu = 4/3$ Chern insulator and Kondo breakdown—To demonstrate the connection between the $\nu = 4/3$ symmetry-broken Chern insulator and Kondo physics, we first show the emergence of heavy fermion physics through temperature- and magnetic-field-dependent transport studies in the mixed-valence region V (Supplemental Material Fig. 2 [27]). In this region, the Fermi level intersects both the W-moiré band and the Mo upper Hubbard band [Fig. 1(d)]. Consistent with earlier results in the Kondo lattice regime [18,22], coherent heavy fermion transport develops at temperatures below the Kondo coherence temperature T^*. A temperature dependence $R_{xx} = R_0 + A \times T^2$ is observed in the low-temperature limit, from which the residual resistance R_0 and the Kadowaki-Woods coefficient A (proportional to the square of the quasiparticle effective mass) can be extracted. For $B > B_C$, the Zeeman energy outcompetes the effective Kondo interaction, leading to a breakdown of the Kondo singlets and the emergence of SdH oscillations due to a drop in the effective mass (Refs. [9,18,22,41]). This is accompanied by a sign change in R_{xy} and a jump in the Hall density, reflecting the reconstruction from a large electronlike Fermi surface to a small holelike Fermi surface (Supplemental Material Fig. 3 [27]). The effective Kondo exchange interaction, as reflected by T^*, $A^{-0.5}$, and B_C, also increases with ν.

With heavy fermion physics established, we show in Figs. 3(a)–3(h) the evolution of the R_{xy} maps versus ν and E with increasing magnetic field. We mark the Kondo breakdown boundary, where R_{xy} changes sign, by dotted lines. The Kondo breakdown boundary extends smoothly from region IV (Kondo lattice region) to region V (mixed-valence region), and moves to higher fillings as the field increases. Interestingly, the R_{xy} hot spot around $\nu = 4/3$ starts to show up as the Kondo breakdown boundary approaches $\nu = 4/3$ in the mixed-valence region. Maximum R_{xy} is observed when the boundary is at a filling slightly less than $\nu = 4/3$, where the R_{xy} hot spot at $\nu = 4/3$ nearly spans the entire mixed-valence region [Figs. 3(c)–3(e)]. The R_{xy} hot spot immediately disappears when the boundary passes $\nu = 4/3$ [Figs. 3(f) and 3(g)]. The abrupt disappearance of the $\nu = 4/3$ state for $B > B_C$ can also be seen in Fig. 2(d). The data show that the $\nu = 4/3$ symmetry-broken Chern insulator becomes the most stable right before the Kondo breakdown, where fluctuation effects are enhanced as the effective Kondo interaction becomes critically weak. The appearance of the $\nu = 4/3$ state only in region V but not in region IV also implies the importance of local-moment fluctuations that are inherent to the mixed-valence region.

Twist angle dependence—We have also systematically measured another device (device II) with a twist angle at 1.5°, which corresponds to $n_M \approx 5.1 \times 10^{12}$ cm^{-2} and $a_M \approx 4.5$ nm. Figures 4(a) and 4(b) show R_{xx} and R_{xy}, respectively, as functions of ν and B at $T = 300$ mK and at a fixed electric field $E = 0.605$ V/nm that cuts through region V at approximately the same location as device I. Compared to device I, the $\nu = 4/3$ Chern insulator appears at higher magnetic fields $5 \lesssim B \lesssim 7$ T; the critical field B_C for Kondo breakdown is also higher. The shift to higher fields could be explained by the higher moiré density n_M, which is expected to enhance the effective Kondo

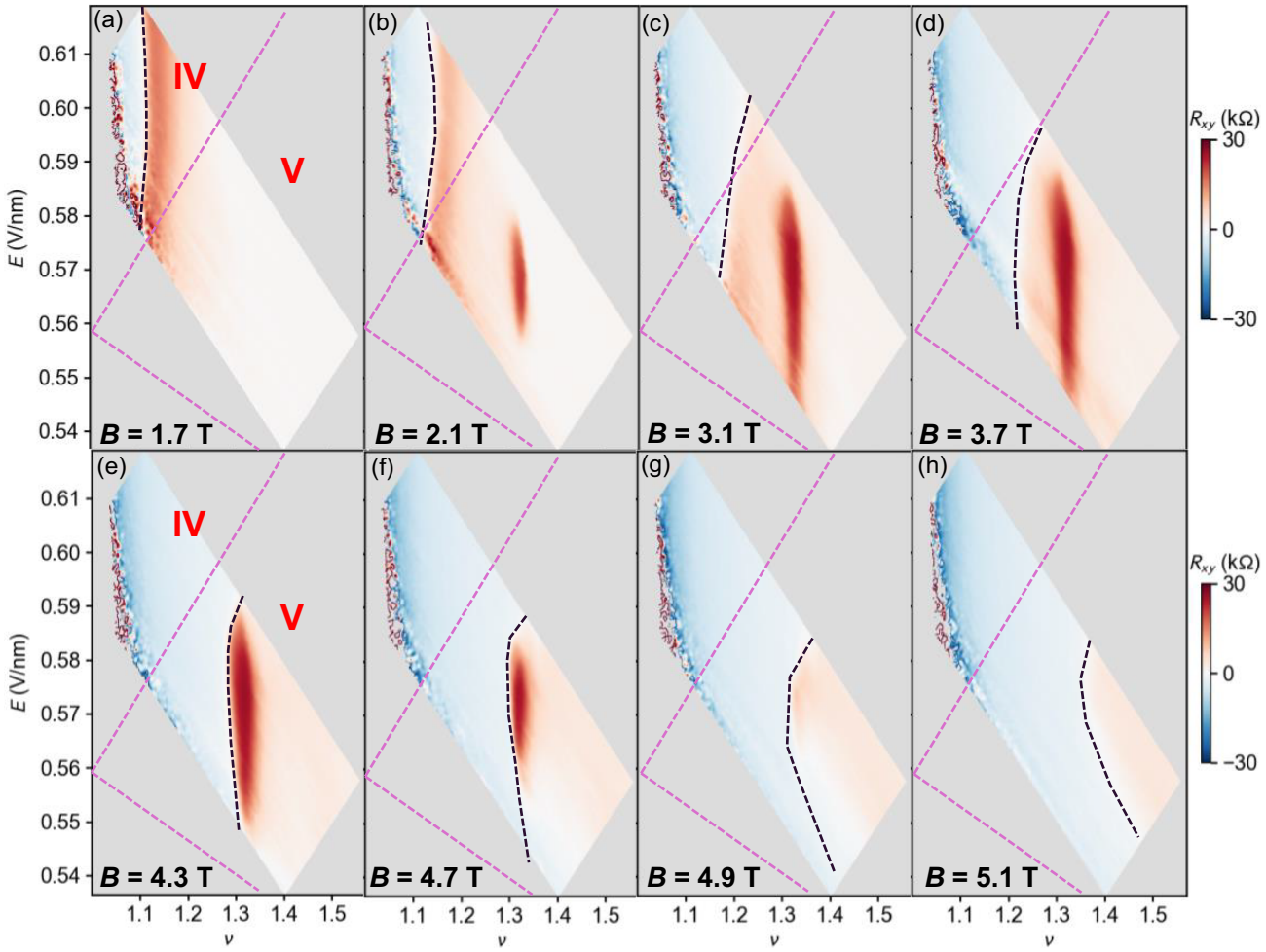


FIG. 3. Evolution of the $\nu = 4/3$ Chern insulator with magnetic field and its connection to Kondo breakdown. (a)–(h) Series of antisymmetrized R_{xy} maps as a function of ν and E with increasing B (values indicated on each panel). Purple dashed lines represent the phase boundaries separating the different regions in the phase diagram. Dotted lines trace the Kondo breakdown boundary (where R_{xy} changes sign). The boundary extends from the Kondo lattice region (IV) into the mixed-valence region (V) and shifts to higher fillings with increasing field.

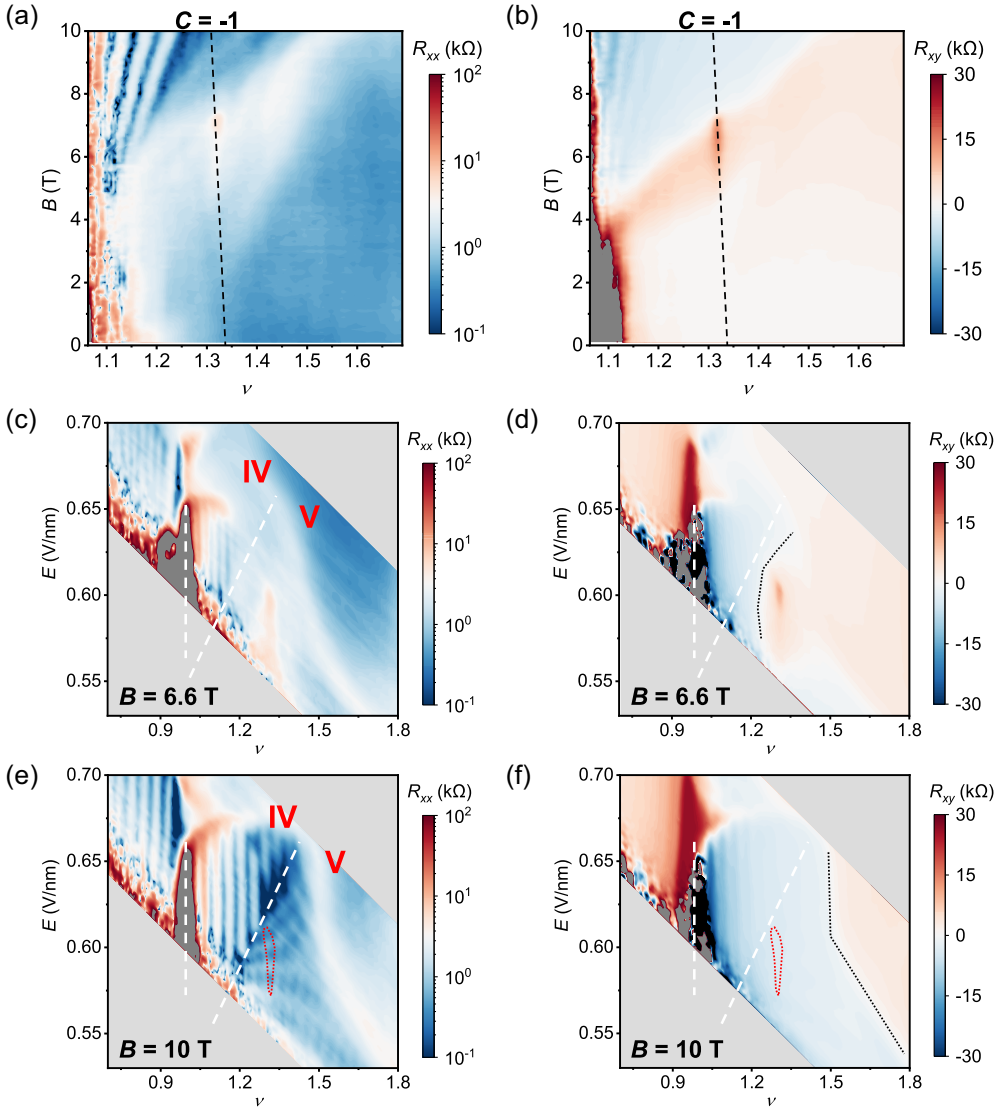


FIG. 4. The $\nu = 4/3$ state in device II with ≈1.5° twist angle. (a) R_{xx} and (b) R_{xy} as functions of ν and B at fixed $E = 0.605$ V/nm. An R_{xy} hot spot emerges near $\nu = 4/3$ for $5 \lesssim B \lesssim 7$ T and disappears suddenly above $B \approx 7$ T. The dashed line marks the dispersion of a $C = -1$ Chern insulator based on the Streda formula. (c)–(f) R_{xx} (c),(e) and antisymmetrized R_{xy} (d),(f) versus ν and E at $B = 6.6$ T (c), (d) and 10 T (e),(f). White dashed lines tentatively mark the phase boundaries for the Kondo lattice (IV) and the mixed-valence (V) regions based on the vertical stripes of SdH oscillations. An R_{xy} hotspot appears near $\nu = 4/3$ at $B = 6.6$ T in region V, close to the Kondo breakdown boundary (black dotted line). The hot spot disappears at $B = 10$ T, where the Kondo breakdown boundary has moved past $\nu = 4/3$. The red dotted contour in (e),(f) marks the R_{xy} hot spot location in (d). All data were measured at $T = 300$ mK.

interaction and the Kondo breakdown critical field [18]. The twist angle dependence of the magnetic field range that hosts the $\nu = 4/3$ state is shown in Supplemental Material Fig. 4 (for a total of four devices) [27]. Whereas the overall field scale increases with the twist angle, the field range decreases slightly.

The R_{xx} and R_{xy} maps versus ν and E of device II at two selected magnetic fields $B = 6.6$ and 10 T are shown in Figs. 4(c)–4(f) (see Supplemental Material Fig. 5 for data at higher fields [27]). Similar to device I, the $\nu = 4/3$ state appears only in the mixed-valence region (region V) and is stabilized only near the Kondo breakdown, whose boundary is marked by black dotted lines in the R_{xy} maps. After the breakdown at $B = 10$ T, two different sets of SdH oscillations crossing each other emerge in region V; the two sets correspond to the two different types of carriers in the system: decoupled holes in the Mo layer and W layer (the former set is less clear in the R_{xx} map due to the heavier effective mass in the Mo layer). These observations further illustrate that the $\nu = 4/3$ symmetry-broken Chern insulator state is intimately linked to the Kondo breakdown, rather than being induced by a change in the band alignment in the two different regions (IV and V).

Whereas the overall behavior of device II is consistent with that of device I, no R_{xx} dip is observed at the R_{xy} hot spot in device II, and the maximum R_{xy} only reaches about 10 kΩ. The absence of a quantized Hall response and the lack of a concurrent R_{xx} dip show that the symmetry-broken Chern insulator at $\nu = 4/3$ is not fully developed in device II, although its dispersion follows the Streda formula with $C = -1$ [shown by dashed lines in Figs. 4(a) and 4(b)]. On the other hand, the QAH state at $\nu = 1$ still shows quantized R_{xy} and vanishing R_{xx} at $T \lesssim 2$ K, demonstrating the reasonably high device quality (Supplemental Material Fig. 6 [27]). These observations suggest that the stability of the $\nu = 4/3$ Chern insulator is highly sensitive to the twist angle, further underscoring the delicate interplay between charge ordering, topology, and the proximity to the Kondo breakdown.

Discussion and outlook—In Supplemental Material Fig. 7 [27], we present a schematic phase diagram of angle-aligned $MoTe_2/WSe_2$ moiré bilayers that summarizes the previously reported phases [19–22,29–31] and incorporates the newly observed symmetry-broken Chern insulator at $\nu = 4/3$ in the mixed-valence regime. The observation of a symmetry-broken Chern insulator near a magnetic-field-induced Kondo breakdown in the mixed-valence region raises many interesting questions for further theoretical and experimental studies. First, although the state emerges at a fractional filling factor, it is an integer rather than a fractional Chern insulator [33,36,42–46]. The observation suggests a rather nonuniform distribution of the Berry curvature for the moiré bands in angle-aligned $MoTe_2/WSe_2$; the nonuniform distribution is likely connected to the dispersive moiré band in the W layer [47]. Second, the emergence of the Chern insulator near the field-induced Kondo breakdown highlights the importance of the chiral Kondo interaction in angle-aligned $MoTe_2/WSe_2$, as pointed out by theoretical studies [23,24]. The chiral Kondo interaction introduces a topological Kondo hybridization gap between the dispersive W-moiré band and the flat Mo-Hubbard band, resulting in topologically protected edge states inside the gap. However, exactly how the topological gap could stabilize a Chern insulator at a fractional filling factor near a Kondo breakdown remains to be theoretically analyzed; in particular, why the $\nu = 4/3$ Chern insulator is only stabilized in the mixed-valence region (region V) but not in the Kondo lattice region (region IV) remains to be better understood. Lastly, the substantially enhanced R_{xx} near the Kondo breakdown [Figs. 1(f), 2(a), and 4(a)] suggests enhanced quasiparticle scattering and/or density of states near the breakdown. Previous studies [18] have also shown that the breakdown is substantially sharpened at low temperatures. These observations suggest that the Kondo breakdown is a quantum phase transition rather than a smooth crossover, as is further supported by a recent thermoelectric study [20]. Whether this transition is quantum critical or not deserves further experimental investigations. Our results motivate further studies of the emergent topological physics in a chiral Kondo system realized in angle-aligned $MoTe_2/WSe_2$.

Acknowledgments—We thank Fengcheng Wu and Yang Zhang for valuable discussions. This work is supported by the National Key R&D Program of China (Grants No. 2022YFA1402702, No. 2022YFA1405400, No. 2021YFA1401300, and No. 2021YFA1401400), the National Natural Science Foundation of China (Grants No. 12350403, No. 12550403, No. 12674229, No. 124B2061, and No. 92265102), the Quantum Science and Technology-National Science and Technology Major Project (Grants No. 2021ZD0302600 and No. 2025ZD0300500), and the Natural Science Foundation of Shanghai (Grants No. 24QA2703700 and No. 24LZ1401100). T. L. acknowledges support from New Cornerstone Science Foundation through the XPLORER grant and support from the Asian Young Scientist Fellowship. S. J. acknowledges the Yangyang Development Fund. K. W. and T. T. acknowledge support from the CREST (Grant No. JPMJCR24A5), JST, and the World Premier International Research Center Initiative, MEXT, Japan. A portion of this work was carried out at the Synergetic Extreme Condition User Facility [48].

Data availability—There are no publicly available research data or software supporting this manuscript. Requests for further information or data should be sent to the authors.

[1] S. Kirchner, S. Paschen, Q. Chen, S. Wirth, D. Feng, J. D. Thompson, and Q. Si, Colloquium: Heavy-electron quantum criticality and single-particle spectroscopy, Rev. Mod. Phys. **92**, 011002(C) (2020).
[2] S. Paschen and Q. Si, Quantum phases driven by strong correlations, Nat. Rev. Phys. **3**, 9 (2021).
[3] G. Stewart, Heavy-fermion systems, Rev. Mod. Phys. **56**, 755 (1984).
[4] V. Vaňo, M. Amini, S. C. Ganguli, G. Chen, J. L. Lado, S. Kezilebieke, and P. Liljeroth, Artificial heavy fermions in a van der Waals heterostructure, Nature (London) **599**, 582 (2021).
[5] G. Li *et al.*, Two-dimensional Fermi surfaces in Kondo insulator SmB_6, Science **346**, 1208 (2014).
[6] M. Dzero, K. Sun, V. Galitski, and P. Coleman, Topological Kondo insulators, Phys. Rev. Lett. **104**, 106408 (2010).
[7] J. Hertz, Quantum critical phenomena, Phys. Rev. B **14**, 1165 (1976).
[8] A. Millis, Effect of a nonzero temperature on quantum critical points in itinerant fermion systems, Phys. Rev. B **48**, 7183 (1993).
[9] P. Gegenwart, Q. Si, and F. Steglich, Quantum criticality in heavy-fermion metals, Nat. Phys. **4**, 186 (2008).

[10] S. Wirth and F. Steglich, Exploring heavy fermions from macroscopic to microscopic length scales, Nat. Rev. Mater. **1**, 16051 (2016).
[11] G. Stewart, Non-Fermi-liquid behavior in d- and f-electron metals, Rev. Mod. Phys. **73**, 797 (2001).
[12] H. Löhneysen, A. Rosch, M. Vojta, and P. Wolfle, Fermi-liquid instabilities at magnetic quantum phase transitions, Rev. Mod. Phys. **79**, 1015 (2007).
[13] J. Mydosh and P. Oppeneer, Colloquium: Hidden order, superconductivity, and magnetism: The unsolved case of URu_2Si_2, Rev. Mod. Phys. **83**, 1301(C) (2011).
[14] M. P. Allan, F. Massee, D. K. Morr, J. Van Dyke, A. W. Rost, A. P. Mackenzie, C. Petrovic, and J. C. Davis, Imaging Cooper pairing of heavy fermions in $CeCoIn_5$, Nat. Phys. **9**, 468 (2013).
[15] L. Jiao, S. Howard, S. Ran, Z. Wang, J. Olivares Rodriguez, M. Sigrist, Z. Wang, N. P. Butch, and V. Madhavan, Chiral superconductivity in heavy-fermion metal UTe_2, Nature (London) **579**, 523 (2020).
[16] W. Simeth *et al.*, A microscopic Kondo lattice model for the heavy fermion antiferromagnet $CeIn_3$, Nat. Commun. **14**, 8239 (2023).
[17] A. Kumar, N. C. Hu, A. H. MacDonald, and A. C. Potter, Gate-tunable heavy fermion quantum criticality in a moiré Kondo lattice, Phys. Rev. B **106**, L041116 (2022).
[18] W. Zhao, B. Shen, Z. Tao, Z. Han, K. Kang, K. Watanabe, T. Taniguchi, K. F. Mak, and J. Shan, Gate-tunable heavy fermions in a moiré Kondo lattice, Nature (London) **616**, 61 (2023).
[19] W. Zhao *et al.*, Emergence of ferromagnetism at the onset of moiré Kondo breakdown, Nat. Phys. **20**, 1772 (2024).
[20] Y. Zhang, W. Zhao, Z. Han, K. Watanabe, T. Taniguchi, J. Shan, and K. F. Mak, Thermoelectricity of moiré heavy fermions in $MoTe_2/WSe_2$ bilayers, Phys. Rev. Lett. **136**, 186501 (2026).
[21] W. Zhao *et al.*, Emergence of Chern metal in a moiré Kondo lattice, arXiv:2506.14063.
[22] Z. Han, Y. Xia, Z. Xia, W. Zhao, Y. Zhang, K. Watanabe, T. Taniguchi, J. Shan, and K. F. Mak, Evidence of topological Kondo insulating state in $MoTe_2/WSe_2$ moiré bilayers, Nat. Phys. **22**, 396 (2026).
[23] D. Guerci, J. Wang, J. Zang, J. Cano, J. H. Pixley, and A. Millis, Chiral Kondo lattice in doped $MoTe_2/WSe_2$ bilayers, Sci. Adv. **9**, eade7701 (2023).
[24] J. Mendez-Valderrama, S. Kim, and D. Chowdhury, Correlated topological mixed-valence insulators in moiré heterobilayers, Phys. Rev. B **110**, L201105 (2024).
[25] F. Xie, L. Chen, and Q. Si, Kondo effect and its destruction in heterobilayer transition metal dichalcogenides, Phys. Rev. Res. **6**, 013219 (2024).
[26] Q. Wu *et al.*, Realization of a Kondo insulator in a multilayer moire superlattice, arXiv:2507.01329.
[27] See Supplemental Material at http://link.aps.org/supplemental/10.1103/szcj-44xj for device fabrication, electrical transport measurements, additional temperature-dependence data, transport evidence of heavy Fermi physics, Kondo breakdown schematics, twist angle dependence, high-field data, and schematic phase diagram.
[28] Z. Han *et al.*, Stacking-order-dependent electronic properties of $MoTe_2/WSe_2$ moiré bilayers, arXiv:2605.21233.
[29] T. Li *et al.*, Quantum anomalous Hall effect from intertwined moiré bands, Nature (London) **600**, 641 (2021).
[30] W. Zhao *et al.*, Realization of the Haldane Chern insulator in a moiré lattice, Nat. Phys. **20**, 275 (2024).
[31] X. Chang *et al.*, Electric-field-tuned consecutive topological phase transitions between distinct correlated insulators in moiré $MoTe_2/WSe_2$ heterobilayer, Phys. Rev. Lett. **136**, 096503 (2026).
[32] L. Wang, Y. Gao, B. Wen, Z. Han, T. Taniguchi, K. Watanabe, M. Koshino, J. Hone, and C. R. Dean, Evidence for a fractional fractal quantum Hall effect in graphene superlattices, Science **350**, 1231 (2015).
[33] E. M. Spanton, A. A. Zibrov, H. Zhou, T. Taniguchi, K. Watanabe, M. P. Zaletel, and A. F. Young, Observation of fractional Chern insulators in a van der Waals heterostructure, Science **360**, 62 (2018).
[34] H. Polshyn *et al.*, Topological charge density waves at half-integer filling of a moiré superlattice, Nat. Phys. **18**, 42 (2021).
[35] Y. Saito, J. Ge, L. Rademaker, K. Watanabe, T. Taniguchi, D. A. Abanin, and A. F. Young, Hofstadter subband ferromagnetism and symmetry-broken Chern insulators in twisted bilayer graphene, Nat. Phys. **17**, 478 (2021).
[36] Y. Xie *et al.*, Fractional Chern insulators in magic-angle twisted bilayer graphene, Nature (London) **600**, 439 (2021).
[37] M. He, J. Cai, Y.-H. Zhang, Y. Liu, Y. Li, T. Taniguchi, K. Watanabe, D. H. Cobden, M. Yankowitz, and X. Xu, Symmetry-broken Chern insulators in twisted double bilayer graphene, Nano Lett. **23**, 11066 (2023).
[38] R. Su, D. Waters, B. Zhou, K. Watanabe, T. Taniguchi, Y.-H. Zhang, M. Yankowitz, and J. Folk, Moiré-driven topological electronic crystals in twisted graphene, Nature (London) **637**, 1084 (2025).
[39] D. Waters *et al.*, Chern insulators at integer and fractional filling in moiré pentalayer graphene, Phys. Rev. X **15**, 011045 (2025).
[40] Z. Zhang *et al.*, Cascade of zero-field Chern insulators in magic-angle bilayer graphene, Natl. Sci. Rev. **13**, nwaf265 (2025).
[41] S. Kitagawa, H. Ikeda, Y. Nakai, T. Hattori, K. Ishida, Y. Kamihara, M. Hirano, and H. Hosono, Metamagnetic behavior and Kondo breakdown in heavy-fermion CeFePO, Phys. Rev. Lett. **107**, 277002 (2011).
[42] J. Cai *et al.*, Signatures of fractional quantum anomalous Hall states in twisted $MoTe_2$, Nature (London) **622**, 63 (2023).
[43] Y. Zeng, Z. Xia, K. Kang, J. Zhu, P. Knüppel, C. Vaswani, K. Watanabe, T. Taniguchi, K. F. Mak, and J. Shan, Thermodynamic evidence of fractional Chern insulator in moiré $MoTe_2$, Nature (London) **622**, 69 (2023).
[44] H. Park *et al.*, Observation of fractionally quantized anomalous Hall effect, Nature (London) **622**, 74 (2023).

[45] F. Xu *et al.*, Observation of integer and fractional quantum anomalous Hall effects in twisted bilayer $MoTe_2$, Phys. Rev. X **13**, 031037 (2023).

[46] Z. Lu, T. Han, Y. Yao, A. P. Reddy, J. Yang, J. Seo, K. Watanabe, T. Taniguchi, L. Fu, and L. Ju, Fractional quantum anomalous Hall effect in multilayer graphene, Nature (London) **626**, 759 (2024).

[47] H. Pan, M. Xie, F. Wu, and S. Das Sarma, Topological Phases in AB-Stacked $MoTe_2/WSe_2$: $\mathbb{Z}_2$ Topological Insulators, Chern Insulators, and Topological Charge Density Waves, Phys. Rev. Lett. **129**, 056804 (2022).

[48] https://cstr.cn/31123.02.SECUF.